PHYSICAL REVIEW A **107**, 043504 (2023)

Zero-energy edge states and solitons in strained photonic graphene

Boquan Ren (任博权),[1] Hongguang Wang (王洪广),[1] Milivoj R. Belić,[2] Yongdong Li (李永东),[1]
Xiaoyu Zhu (朱小宇),[3] and Yiqi Zhang (张贻齐)[1,*]

[1]*Key Laboratory for Physical Electronics and Devices of the Ministry of Education and Shaanxi Key Lab of Information Photonic Technique, School of Electronic and Information Engineering, Xi'an Jiaotong University, Xi'an 710049, China*
[2]*Division of Arts and Sciences, Texas A&M University at Qatar, P.O. Box 23874, Doha, Qatar*
[3]*School of Physics, MOE Key Laboratory for Non-equilibrium Synthesis and Modulation of Condensed Matter, Xi'an Jiaotong University, Xi'an 710049, China*

(Received 9 December 2022; revised 15 February 2023; accepted 28 March 2023; published 14 April 2023)

Photonic graphene is a form of graphene in optic platforms that is important for fabrication of photonic topological insulators, which may lead to novel techniques to realize various types of light manipulation. Among a plethora of schemes to reform photonic graphene to meet the desired specifications, the significance of strain operations has not received sufficient attention. Here, we theoretically and numerically report zero-energy edge states in strained photonic graphene. After applying strain, photonic graphene can be regarded as a stack of Su-Schrieffer-Heeger chains, which can be considered to be a convincing cause of the appearance of zero-energy edge states. In addition, the topological origin is analyzed based on the tight-binding method, and we find that the Zak phase is π when there is a zero-energy edge state. In reference to the dispersive nature of zero-energy edge states, the self-action effect of nonlinearity is introduced to balance the dispersive broadening of these states to form both bright and dark zero-energy edge solitons. We believe that the results obtained may provide deeper understanding of the role of strain in two-dimensional lattices and may find potential applications in fabricating future on-chip on-demand photonic devices.

DOI: 10.1103/PhysRevA.107.043504

I. INTRODUCTION

Photonic graphene, which is also called the honeycomb lattice, is a form of graphene that can be easily adopted to manipulate the propagation of light [1–3]. It also provides an ideal platform for realizing photonic topological insulators [4–7]. It is well known that photonic graphene can be elaborately cut to realize zigzag, bearded, and armchair boundary terminations. Without any procedure to break the original symmetry of photonic graphene, only zigzag and bearded terminations can support edge states [8]. The edge state of the zigzag termination is at the boundary of the first Brillouin zone (BZ), while that of the bearded termination is in the middle of the zone. That means that the edge state of a single-type termination does not completely fill the full width of the first BZ of photonic graphene, even though certain symmetries are broken [4,9,10]. However, we occasionally find that photonic graphene strained in certain fashions may reverse this traditional perception. The counterintuitive appearance of the edge state in the whole first BZ that we discuss later can be explained by using the Su-Schrieffer-Heeger (SSH) model [11–13], which is the simplest model and also well recognized for topological insulators.

It has been demonstrated in many fields of physics that straining a lattice can produce a pseudomagnetic field (also referred to as an artificial magnetic field, synthetic magnetic field, effective magnetic field, or gauge field) and also Landau levels [14–22]. It has also been reported that the straining operation may help restore the parity-time symmetry [23,24]. Especially, it was reported that edge states are created on the zigzag edge and destroyed on the bearded edge by compression in the vertical direction of photonic graphene [25]. Without a doubt, strain is a useful tool for studying topological physics [26–28] and deserves more attention.

In this work, we investigate zero-energy edge states [29–32] in strained photonic graphene and report bright and dark zero-energy edge solitons. We regard photonic graphene as a stack of horizontal or vertical chains, and to strain photonic graphene, we decrease the separation distance between the chains. In this way, the coupling strengths of one site and its three nearest-neighbor sites, which are identical before straining, are not the same any longer. If the strained photonic graphene is still regarded as a stack of horizontal chains, one finds that the coupling strength of each pair of nearest-neighbor sites alternately changes between strong and weak values. This staggered coupling strength is the same as that of an SSH chain, so the strained photonic graphene is equivalent to the stacked SSH chain. This operation is different from strain reported in previous studies [25,33], even though it can also lead to merging and annihilation of Dirac points. For photonic graphene with zigzag-bearded terminations (that support edge states on both terminations simultaneously before straining) one may expect only one of them (either the zigzag termination or the bearded termination) to support edge states after straining. We believe this is another counterintuitive phenomenon unveiled in this work. To understand the topological origin of such zero-energy edge states, the tight-

---

[*] zhangyiqi@xjtu.edu.cn

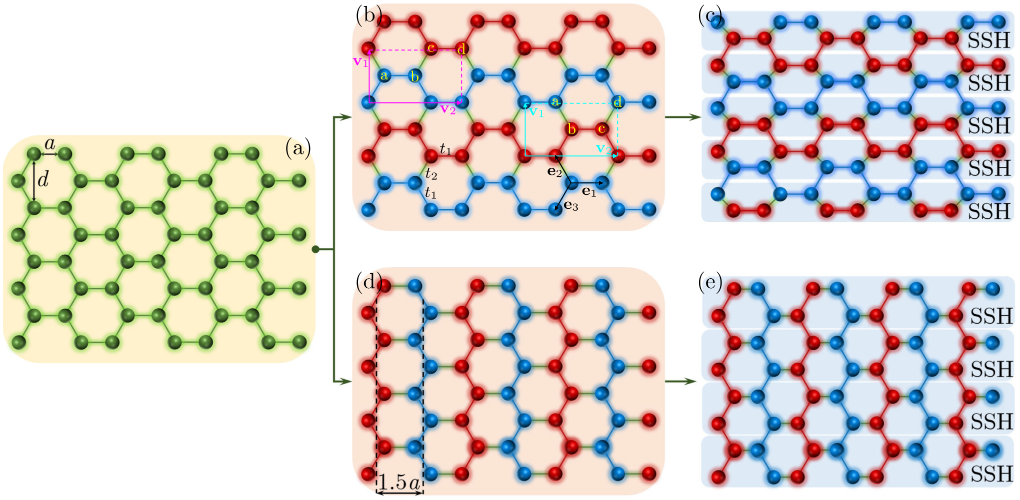

FIG. 1. (a) Regular photonic graphene. (b) The regular photonic graphene is regarded as a formation of stacked horizontal chains represented in red and blue. The separation distance between two neighboring chains is $d = \sqrt{3}a$, with a being the lattice constant of each chain. Typical vectors for the tight-binding method are $\mathbf{e}_1 = [a, 0]$, $\mathbf{e}_2 = [-a/2, d/2]$, and $\mathbf{e}_3 = [-a/2, -d/2]$, and the basis vectors of the Bravais lattice are $\mathbf{v}_1 = [0, d]$ and $\mathbf{v}_2 = [3a, 0]$. As shown by the cyan and magenta rectangles, the four sites in one unit cell can be chosen in two different ways. The coupling strength between sites connected by red and blue bonds is t_1, and that with green bond is t_2. (c) The separation distance between horizontal chains is squeezed, and SSH chains are established (highlighted with shading), so that the zero state will appear on the right bearded termination of the lattice. (d) The regular photonic graphene is regarded as a formation of stacked vertical chains with a separation distance of $1.5a$. (e) Decreasing the separation distance also leads to SSH chains with the zero-energy state appearing on the left zigzag termination.

binding method is utilized to analyze the strained photonic graphene. Based on the zero-energy edge states, we superpose soliton envelops on them and obtain bright and dark zero-energy edge solitons. The stability of these zero-energy edge solitons is also discussed by introducing a small perturbation and monitoring long-distance propagation.

We would like to note that the tight-binding method is used only to understand the topological origin of the zero-energy edge state, and other results shown in this work are obtained directly based on the continuous model (i.e., the Schrödinger-like paraxial wave equation), which is closer to real-world conditions and more useful for experimentalists.

II. RESULTS AND DISCUSSION

A. Theoretical model

Generally, the propagation dynamics of a light beam can be well described by the nonlinear Schrödinger-like equation with focusing cubic nonlinearity for the dimensionless light field amplitude ψ:

$$i\frac{\partial\psi}{\partial z} = -\frac{1}{2}\left(\frac{\partial^2}{\partial x^2} + \frac{\partial^2}{\partial y^2}\right)\psi - \mathcal{R}(x, y)\psi - |\psi|^2\psi. \quad (1)$$

Here, x and y are the normalized transverse coordinates, and z is the propagation distance. The function $\mathcal{R}(x, y)$ describes the waveguide array, which is independent of z (namely, the waveguide array is straight along z axis), and it can be written as

$$\mathcal{R}(x, y) = p\sum_{m,n}\exp\left[-\frac{(x - x_m)^2 + (y - y_n)^2}{\sigma^2}\right], \quad (2)$$

where (x_m, y_n) are the coordinates of the lattice sites, p is the depth of the lattice that is proportional to the refractive index modulation depth, and σ is the waveguide width. Photonic graphene with zigzag-bearded terminations in x is displayed in Fig. 1(a), in which a is the lattice constant and $d = \sqrt{3}a$ is the period in y. We use the parameters $a = 1.6$, $\sigma = 0.5$, and $p = 8$, which are representative of femtosecond laser-written waveguide arrays [13,34–36]. Note that the waveguide array can also be induced in photorefractive crystals [37–39] and atomic vapors [40–42], where one has to switch the nonlinearity in Eq. (1) from cubic type to saturable type. Taking the potential sample fabricated by using the femtosecond laser-direct-writing technique as an example, real physical parameters for a, σ, and p are ~16 μm, ~5 μm, and a refractive index change of $\sim 0.9 \times 10^{-3}$, respectively, if a beam with a wavelength of 800 nm is adopted.

First, photonic graphene can be regarded as a stack of horizontal armchair chains. To better illustrate this idea, we mark the horizontal armchair chains in red and blue, as shown in Fig. 1(b). Since we do not deform the photonic graphene in Fig. 1(b), the period in y is still d, which can be referred to as the separation of neighboring horizontal armchair chains. Now, we decrease the separation and meanwhile keep the profile of each chain unchanged. The resultant strained photonic lattice is exhibited in Fig. 1(c), which is C_2 symmetric. We find that the top sites from the red chain are closer to the bottom sites from the blue chain, and the top sites from the blue chain are closer to the bottom sites from the red chain. If we rearrange the components of stacked chains, e.g., top sites from the red (blue) chain and bottom sites from the blue (red) chain, as highlighted by light blue shading in Fig. 1(c), the coupling strength between two neighboring sites in each chain alternately becomes strong and weak. Obviously, each

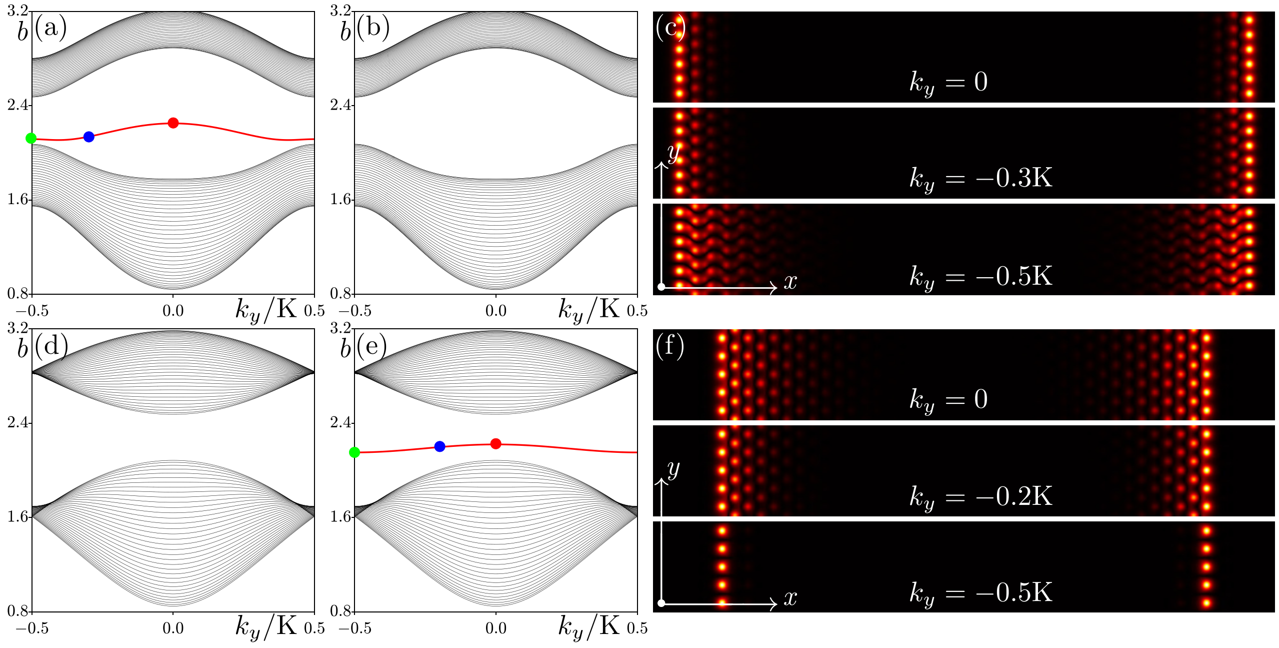

FIG. 2. (a) Band structure corresponding to the case shown in Fig. 1(c) with $d = \sqrt{2}a$. The lattice is periodic along y but limited along x with bearded terminations. There are two degenerate zero-energy states (red curve) in the band gap. (b) Same as (a), but for the lattice with zigzag terminations. There is no zero-energy state in the band gap. (c) Modulus profiles of the selected zero-energy edge state that correspond to the dots in (a). (d) Band structure corresponding to the case shown in Fig. 1(e) with a separation of $1.25a$. The lattice is periodic along y but limited along x with bearded terminations. There is no zero-energy state in the band gap. (e) Same as (d), but for the lattice with a zigzag on both terminations. There are two degenerate zero-energy states (red curve) in the band gap. (f) Modulus profiles of the selected zero-energy edge state that correspond to the dots in (e). Panels in (c) and (f) are shown in regions where $-48 \leqslant x \leqslant 48$ and $-7 \leqslant y \leqslant 7$.

chain is, in essence, an SSH chain. It is well known that a topological state can be found at the end of the SSH chain where the coupling between two end sites is weak, and the corresponding topological phase transition can be depicted by the winding number [11]. Therefore, one expects an edge state at the bearded termination.

Second, photonic graphene can also be regarded as a stack of vertical zigzag chains, as shown in Fig. 1(d). Upon decreasing the separation among vertical zigzag chains from $1.5a$, similar strained SSH chains can be established, as shown in Fig. 1(e). Different from the case in Fig. 1(c), one expects an edge state at the zigzag termination.

B. Band structures and zero-energy edge states

One significant step is to check the band structure of the strained photonic graphene in Figs. 1(c) and 1(e). To this end, we neglect the nonlinear term in Eq. (1) and search for the eigenmodes of the structure in the form $\psi = u(x, y)\exp(ik_y y + ibz)$, with b being the propagation constant (an eigenvalue); $-0.5\,\mathrm{K} \leqslant k_y \leqslant 0.5\,\mathrm{K}$, where $\mathrm{K} = 2\pi/d$, being the width of the first BZ; and $u(x, y)$ being the modal field. As a result, we obtain from Eq. (1) the linear eigenvalue problem

$$bu = \frac{1}{2}\left(\frac{\partial^2}{\partial x^2} + \frac{\partial^2}{\partial y^2} + 2ik_y\frac{\partial}{\partial y} - k_y^2\right)u + \mathcal{R}u, \qquad (3)$$

which can be solved numerically using the plane-wave expansion method.

We first consider a case similar to that shown in Fig. 1(c). In Fig. 2(a), we display the band structure of the lattice with bearded-bearded terminations. We find that there are zero-energy edge states in the band gap, as highlighted by the red curve. As a comparison, we also display the band structure of the same lattice but with the zigzag-zigzag terminations in Fig. 2(b), and we find a vacant band gap. The numerical results agree with our previous qualitative analysis that the zero-energy edge state appears only at the bearded and not at the zigzag terminations. The panels in Fig. 2(c) represent modulus profiles of the selected zero-energy edge states that correspond to the dots in Fig. 2(a). We find that the localization of the zero-energy edge state in the boundary area of the first BZ is not as good as that in the middle area since it is closer to the bulk band. For a case similar to that shown in Fig. 1(e), we display the results in Figs. 2(d)–2(f). Again, the numerical results are in accordance with what was analyzed before; that is, the zero-energy edge state appears only at the zigzag terminations [Fig. 2(e)] and is absent at the bearded terminations [Fig. 2(d)]. The localization of the zero-energy edge state in Fig. 2(e) is also the opposite of that in Fig. 2(a)—the localization is better in the boundary area of the first BZ.

C. Topological origin of the zero-energy edge state based on the tight-binding method

We take the lattice type displayed in Figs. 1(c) as an example. According to the quantities set in Fig. 1(b), the bulk

Hamiltonian can be written as

$$\mathcal{H}=\begin{bmatrix} 0 & t_1e^{-i\mathbf{k}\cdot\mathbf{e}_3}+t_2e^{-i\mathbf{k}\cdot\mathbf{e}_2} & 0 & t_1e^{-i\mathbf{k}\cdot\mathbf{e}_1} \\ t_1e^{+i\mathbf{k}\cdot\mathbf{e}_3}+t_2e^{+i\mathbf{k}\cdot\mathbf{e}_2} & 0 & t_1e^{+i\mathbf{k}\cdot\mathbf{e}_1} & 0 \\ 0 & t_1e^{-i\mathbf{k}\cdot\mathbf{e}_1} & 0 & t_1e^{-i\mathbf{k}\cdot\mathbf{e}_2}+t_2e^{-i\mathbf{k}\cdot\mathbf{e}_3} \\ t_1e^{+i\mathbf{k}\cdot\mathbf{e}_1} & 0 & t_1e^{+i\mathbf{k}\cdot\mathbf{e}_2}+t_2e^{+i\mathbf{k}\cdot\mathbf{e}_3} & 0 \end{bmatrix}, \tag{4}$$

with $\mathbf{k}=[k_x,k_y]$ if only the nearest-neighbor coupling is considered. The Hamiltonian can also be written as

$$\mathcal{H}=\begin{bmatrix} 0 & t_1 & 0 & t_2e^{+i\mathbf{k}\cdot\mathbf{v}_2}+t_1e^{+i\mathbf{k}\cdot(\mathbf{v}_1+\mathbf{v}_2)} \\ t_1 & 0 & t_2+t_1e^{+i\mathbf{k}\cdot\mathbf{v}_1} & 0 \\ 0 & t_2+t_1e^{-i\mathbf{k}\cdot\mathbf{v}_1} & 0 & t_1 \\ t_2e^{-i\mathbf{k}\cdot\mathbf{v}_2}+t_1e^{-i\mathbf{k}\cdot(\mathbf{v}_1+\mathbf{v}_2)} & 0 & t_1 & 0 \end{bmatrix} \tag{5}$$

if the unit cell is chosen to be the magenta rectangle with Bravais vectors $\mathbf{v}_{1,2}$ in Fig. 1(b) or

$$\mathcal{H}=\begin{bmatrix} 0 & t_1e^{-i\mathbf{k}\cdot\mathbf{v}_1}+t_2 & 0 & t_1e^{+i\mathbf{k}\cdot\mathbf{v}_2} \\ t_1e^{+i\mathbf{k}\cdot\mathbf{v}_1}+t_2 & 0 & t_1 & 0 \\ 0 & t_1 & 0 & t_1e^{+i\mathbf{k}\cdot\mathbf{v}_1}+t_2 \\ t_1e^{-i\mathbf{k}\cdot\mathbf{v}_2} & 0 & t_1e^{-i\mathbf{k}\cdot\mathbf{v}_1}+t_2 & 0 \end{bmatrix} \tag{6}$$

if the unit cell is chosen to be the cyan rectangle with Bravais vectors $\mathbf{v}_{1,2}$ in Fig. 1(b).

Clearly, the bulk Hamiltonian is translationally invariant, and there is chiral symmetry, which is a condition for the existence of zero-energy edge states [29]. By diagonalizing the bulk Hamiltonian, we obtain the eigenvalues

$$b_{1\sim4}(k_x,k_y)=\pm\sqrt{f^2\pm2ft_1\cos\left(\frac{3}{2}ak_x\right)+t_1^2}, \tag{7}$$

with $f^2=2t_1t_2\cos(\sqrt{3}ak_y)+t_1^2+t_2^2$, which are band structures of the lattice system. Considering that $b_{2,3}$ touch each other through Dirac points if strain is not strong, the value of $b_{2,3}$ is zero at the Dirac points. According to Eq. (7), it is simple to conclude that the Dirac points distribute along $k_x=0$. As a result, we obtain the following relation from $b_{2,3}=0$:

$$\frac{t_2}{2t_1}=-\cos(\sqrt{3}ak_y), \tag{8}$$

which reflects that Dirac points always exist for the case with $t_2<2t_1$ if $|k_y|>\pi/2\sqrt{3}a$ is properly chosen. The Dirac points move toward the boundary of the Brillouin zone with $t_2/2t_1$ increasing gradually and disappear if $t_2/2t_1>1$. In other words, a band gap always exists if $t_2>2t_1$, where a zero-energy edge state can be expected for certain boundaries. Numerical simulations demonstrate the above deduction. In light of the above discovery, it is safe and also reasonable to set $t_1=0.5$ and $t_2=1.5$ for further discussion.

According to the bulk-edge correspondence principle [29], we choose the unit cell shown by the magenta rectangle in Fig. 1(b) [the corresponding Hamiltonian is given in Eq. (5)] for the case with bearded-bearded boundaries and the cyan rectangle [the corresponding Hamiltonian is given in Eq. (6)] for the case with zigzag-zigzag boundaries. We calculate the corresponding Zak phase of the strain lattice with certain boundaries by scanning the Bloch momentum k_y, which is similar to a one-dimensional system [30]. The Zak phase $\mathcal{Z}(k_y)$ can be calculated by using the Wilson-loop method [43]. It is simple to check that there are two bands below the band gap, so we have to construct a 2×2 matrix with elements

$$F_{mn}^{k_{x,j},k_{x,j+1}}=\langle u_m(k_{x,j})|u_n(k_{x,j+1})\rangle, \tag{9}$$

where $|u_{m,k_j}\rangle$ is the Bloch function corresponding to the mth band, where $k_{x,j}\in[-\pi/3a,\pi/3a]$, $k_{x,j+1}=k_{x,j}+\delta k$, $\delta k=(2\pi/3a)/N$, j ranges from 1 to N, and $k_{x,N+1}=k_{x,1}$ if the Brillouin zone is equally divided into N sections. The Berry phase for a loop in the Brillouin zone $[-\pi/3a,\pi/3a]$ can be obtained by the matrix product of the 2×2 matrices for the small segments in the loop with the following form:

$$W=\prod_{j=1}^{j=N}F_{mn}^{k_{x,j},k_{x,j+1}}. \tag{10}$$

Diagonalizing the matrix in Eq. (10), we obtain the corresponding eigenvalues $\exp(i\theta_1)$ and $\exp(i\theta_2)$, and the Zak phase is $\mathcal{Z}=\theta_1+\theta_2$. We show the results in Fig. 3 for the system with different boundaries. If the boundary is the bearded-bearded type, there is always a zero-energy edge state in the band gap, and the Zak phase should always be π for any k_y, which is indeed the case, as shown in Fig. 3(a). However, if

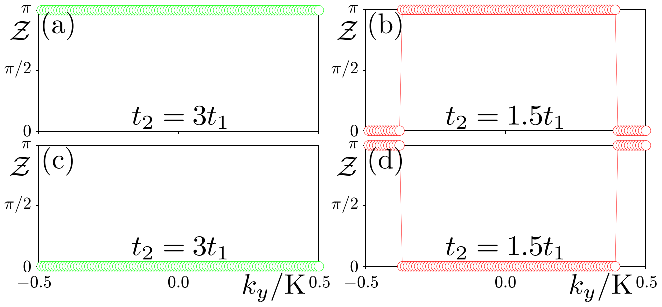

FIG. 3. (a) Zak phase of the system with bearded-bearded boundaries and $t_2=3t_1$. (b) Zak phase of the system with bearded-bearded boundaries and $t_2=1.5t_1$. (c) Zak phase of the system with zigzag boundaries and $t_2=3t_1$. (d) Zak phase of the system with zigzag boundaries and $t_2=1.5t_1$.

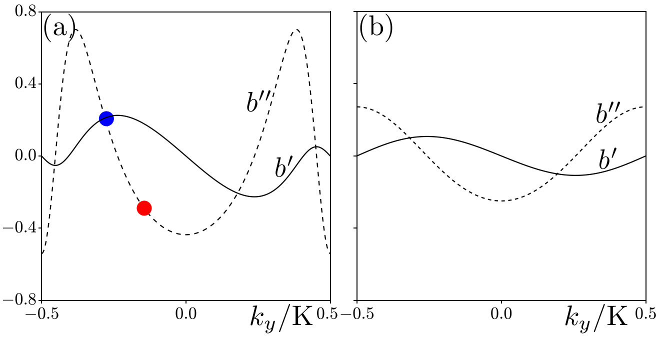

FIG. 4. (a) First-order b' (solid curve) and second-order b'' (dashed curve) derivatives of the zero-energy edge state [corresponding to Fig. 2(a)]. Red and blue dots are at $k_y = -0.16\,\mathrm{K}$ and $k_y = -0.29\,\mathrm{K}$, respectively. (b) Same as (a), but corresponding to Fig. 2(e).

the boundary is the zigzag-zigzag type, there is no zero-energy edge state in the gap, and the Zak phase is always zero, as shown in Fig. 3(c). In Figs. 3(b) and 3(d), we show two cases with $t_2 < 2t_1$ in which there are still Dirac points. We find that zero-energy edge states can appear at both bearded and zigzag boundaries, but their existence ranges are complementary.

D. Zero-energy edge solitons

The zero-energy edge state is so named in this work due its energy being zero, and meanwhile, it is dispersion free if it is analyzed by the tight-binding method with only the nearest-neighbor coupling being considered. However, the zero-energy edge state is generally dispersive when it is based on the continuous model (i.e., the Schrödinger-like equation), which can be seen from the red curves in Figs. 2(a) and 2(e). We calculate the first-order derivative $b' = db/dk_y$ and the second-order derivative $b'' = d^2b/dk_y^2$ of the zero-energy edge state with respect to the Bloch momentum k_y, and the results are shown in Fig. 4. We find that the second-order derivative b'' can be either positive or negative for lattices with both bearded-bearded terminations [Fig. 4(a)] and zigzag-zigzag terminations [Fig. 4(b)], depending on the Bloch momentum. As demonstrated previously, one can expect to have bright edge solitons if $b'' < 0$ and dark edge solitons if $b'' > 0$ [9,10,37,44,45]. Here, we take the first case with bearded-bearded terminations as the topic of investigation and construct a bright zero-energy edge soliton on the bearded termination and a dark zero-energy edge soliton on the other.

To construct zero-energy edge solitons, we adopted the method developed in previous studies [44,46], according to which the soliton can be prepared by superposing the envelopes onto the linear zero-energy edge state. The envelope equation corresponding to Eq. (1) can be written as

$$i\frac{\partial A}{\partial z} = \frac{b''}{2}\frac{\partial^2 A}{\partial Y^2} - \chi |A|^2 A, \tag{11}$$

where A is the slowly varying envelope;

$$\chi = \int_{-\infty}^{+\infty} dx \int_0^L |\phi|^4 dy$$

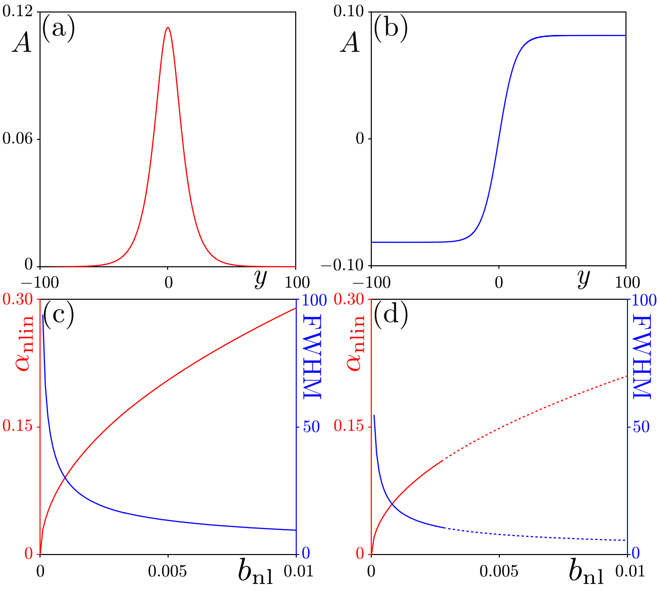

FIG. 5. (a) Bright zero-energy edge soliton envelope with $b_{\mathrm{nl}} = 0.0015$. (b) Same as (a), but for the dark zero-energy edge soliton. (c) Peak amplitude of the bright envelope versus b_{nl} (red curve and left y axis) and FWHM of the envelope (blue curve and right y axis). (d) Amplitude of the background of the dark envelope versus b_{nl} (red curve and left y axis) and FWHM of the envelope (blue curve and right y axis). Dashed lines in (d) represent unstable zero-energy edge solitons constructed based on these envelopes.

is the nonlinearity coefficient, with L being the period in y; and $Y = y + b'z$. The soliton solution can be written in the form $\psi(x, y, z) = A(Y, z)\phi(x, y)\exp(ibz)$, in which $\phi(x, y)\exp(ibz)$ is the linear Bloch state. Equation (11) is the well-known nonlinear Schrödinger equation with third-order nonlinearity (i.e., Kerr nonlinearity), and it possesses numerous solutions. We are interested in the soliton solutions that can be written as [10,44,45]

$$A(y, z) = \sqrt{2\frac{b_{\mathrm{nl}}}{\chi}}\,\mathrm{sech}\left(\sqrt{-2\frac{b_{\mathrm{nl}}}{b''}}(y + b'z)\right)\exp(ib_{\mathrm{nl}}z) \tag{12}$$

for bright solitons and

$$A(y, z) = \sqrt{\frac{b_{\mathrm{nl}}}{\chi}}\tanh\left(\sqrt{\frac{b_{\mathrm{nl}}}{b''}}(y + b'z)\right)\exp(ib_{\mathrm{nl}}z) \tag{13}$$

for dark solitons, where b_{nl} is the nonlinearity-induced phase shift, which should be sufficiently small. In Figs. 5(a) and 5(b), we show exemplary envelopes for the bright and dark solitons with $b_{\mathrm{nl}} = 0.0015$, respectively. Furthermore, we also display the peak amplitude and the FWHM of the bright envelope as a function of b_{nl} in Fig. 5(c). We find that the peak amplitude of the envelope increases with b_{nl}, but the FWHM decreases. In Fig. 5(d), the background amplitude of the dark envelope and the FWHM are shown, and we find that the notch will become narrower with larger b_{nl}.

Zero-energy edge solitons are obtained by superposing these envelopes onto the normalized linear zero-energy edge states for proper Bloch momenta. In Fig. 6(a), we display

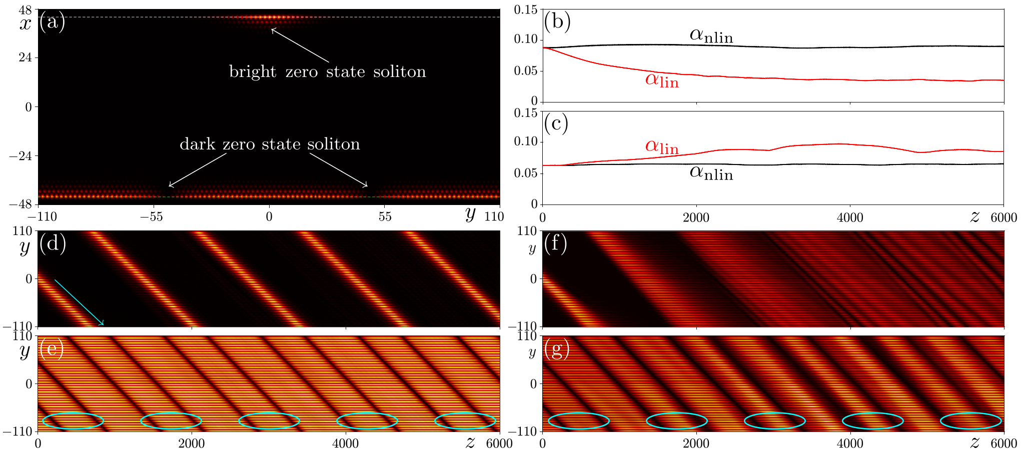

FIG. 6. (a) Constructed bright and dark zero-energy edge solitons at two bearded terminations. (b) Peak amplitude of the bright zero-energy edge soliton during nonlinear propagation ($\alpha_{\rm nlin}$; black curve) and linear propagation ($\alpha_{\rm lin}$; red curve). (c) Peak amplitude of the dark zero-energy edge soliton during nonlinear propagation ($\alpha_{\rm nlin}$; black curve) and linear propagation ($\alpha_{\rm lin}$; red curve). (d) Amplitude distribution of the bright zero-energy edge soliton [along the white dashed line in (a)] during propagation at $k_y = -0.16\,\mathrm{K}$ with $b'' = -0.2549$. (e) Amplitude distribution of the dark zero-energy edge soliton [along the green dashed line in (a)] during propagation at $k_y = -0.29\,\mathrm{K}$ with $b'' = 0.2644$. Two dark zero-energy edge solitons are indicated by cyan ellipses. (f) and (g) Same as (d) and (e), but for linear propagation. $b_{\rm nl} = 0.0015$.

one bright zero-energy edge soliton and one dark zero-energy edge soliton on strained photonic graphene with bearded-bearded terminations. The bright zero-energy edge soliton corresponds to the red dot ($k_y = -0.16$K) in Fig. 4(a), while the dark zero-energy edge soliton corresponds to the blue dot ($k_y = -0.29$K) in Fig. 4(a). We inspect the nonlinear propagation dynamics of the bright (dark) soliton and record the corresponding peak amplitude (the background amplitude) $\alpha_{\rm nlin}$ during propagation, as shown by the black curve in Fig. 6(b) [Fig. 6(c)]. Clearly, the peak amplitude does not change even after a long propagation distance $z \sim 6000$, which verifies the self-trapping of the beam due to the self-action effect of the cubic nonlinearity. If the nonlinearity is lifted, the beam will undergo a linear propagation, and the corresponding peak amplitude (the background amplitude) $\alpha_{\rm lin}$ is indicated by the red curve in Fig. 6(b) [Fig. 6(c)]. For the linear propagation of the bright soliton, the peak amplitude decreases with distance, while for the dark soliton the background increases. Both red curves imply broadening of the incident localized structures during propagation.

To better see the comparison between nonlinear propagation and linear propagation, we record the beam in cross sections indicated by the dashed lines in Fig. 6(a). Figure 6(d) is the bright soliton, and we find that the pattern does not change during propagation. The bright soliton exhibiting a section-by-section dynamics is due to the propagation method we utilized, which is the split-step Fourier method. The soliton propagates in the direction indicated by the cyan arrow in Fig. 6(d), and it will reappear in the opposite boundary when it reaches the boundary of the calculation window. The dark soliton in the cross section shown in Fig. 6(e) behaves similarly—the two dark notches that are marked with cyan ellipses maintain their shapes very well during propagation. The linear counterparts are shown in Figs. 6(f) and 6(g); we find that the hump or the notch of the beam broadens explicitly during propagation, which is different from the nonlinear propagation in Figs. 6(d) and 6(e).

Last, but not least, we check the stability of zero-energy edge solitons by superposing a random noise on incident beams and then propagating over a long distance $z \sim 6000$. The maximum strength of the perturbation is 10% of the peak amplitude (or the background amplitude) of the beam. If the profile of the soliton does not change, then we call it the stable soliton [47]. Otherwise, it is unstable. Results are shown in Figs. 5(c) and 5(d), and unstable solitons are illustrated by dashed lines. We find that the bright zero-energy edge soliton is always stable, while for the dark zero-energy edge soliton the threshold value is $b_{\rm nl}^{\rm th} \sim 0.0028$, above which the dark zero-energy edge soliton is unstable. We would like to note that the metastable region of zero-energy edge solitons is also affected by the Bloch momentum, and zero-energy edge solitons corresponding to other Bloch momenta can be analyzed in the same way.

III. CONCLUSION

In conclusion, we have investigated the zero-energy edge states and zero-energy edge solitons in photonic graphene after a strain operation which makes the photonic graphene equivalent to a stack of SSH chains. The appearance of such zero-energy edge states can be well predicted by the properties of the SSH model. Based on the zero-energy edge state, bright and dark zero-energy edge solitons are obtained by superposing corresponding envelopes. Since the same termination supports both bright and dark zero-energy edge solitons, the strained photonic graphene reported in this work would also be effective in the search for various vector zero-energy edge solitons [44–46,48,49]. It is worth noting that strained photonic graphene can also be useful for investigating higher-order topological insulators, which possess zero-dimensional corner states [34,50,51] that are crucial for developing corner lasing [52–55] and preparing high-quality topological cavities [56,57]. We believe that our results not only provide an ideal platform for investigating topological physics phenomena but also exhibit potential applications for developing compact optical functional devices.

ACKNOWLEDGMENTS

This research was funded by the National Natural Science Foundation of China (Grants No. 12074308 and No. U1537210), the Fundamental Research Funds for the Central Universities (Grant No. xzy022022058), and the NPRP 12S-0205-190047 project from the Qatar National Research Fund (a member of the Qatar Foundation).

---

[1] O. Peleg, G. Bartal, B. Freedman, O. Manela, M. Segev, and D. N. Christodoulides, Conical Diffraction and Gap Solitons in Honeycomb Photonic Lattices, Phys. Rev. Lett. **98**, 103901 (2007).
[2] M. J. Ablowitz, S. D. Nixon, and Y. Zhu, Conical diffraction in honeycomb lattices, Phys. Rev. A **79**, 053830 (2009).
[3] D. Song, V. Paltoglou, S. Liu, Y. Zhu, D. Gallardo, L. Tang, J. Xu, M. Ablowitz, N. K. Efremidis, and Z. Chen, Unveiling pseudospin and angular momentum in photonic graphene, Nat. Commun. **6**, 6272 (2015).
[4] M. C. Rechtsman, J. M. Zeuner, Y. Plotnik, Y. Lumer, D. Podolsky, F. Dreisow, S. Nolte, M. Segev, and A. Szameit, Photonic Floquet topological insulators, Nature (London) **496**, 196 (2013).
[5] L.-H. Wu and X. Hu, Scheme for Achieving a Topological Photonic Crystal by Using Dielectric Material, Phys. Rev. Lett. **114**, 223901 (2015).
[6] J. Noh, S. Huang, K. P. Chen, and M. C. Rechtsman, Observation of Photonic Topological Valley Hall Edge States, Phys. Rev. Lett. **120**, 063902 (2018).
[7] J. Noh, W. A. Benalcazar, S. Huang, M. J. Collins, K. P. Chen, T. L. Hughes, and M. C. Rechtsman, Topological protection of photonic mid-gap defect modes, Nat. Photonics **12**, 408 (2018).
[8] Y. Plotnik, M. C. Rechtsman, D. Song, M. Heinrich, J. M. Zeuner, S. Nolte, Y. Lumer, N. Malkova, J. Xu, A. Szameit, Z. Chen, and M. Segev, Observation of unconventional edge states in ‘photonic graphene,’ Nat. Mater. **13**, 57 (2014).
[9] Q. Tang, B. Ren, V. O. Kompanets, Y. V. Kartashov, Y. Li, and Y. Zhang, Valley Hall edge solitons in a photonic graphene, Opt. Express **29**, 39755 (2021).
[10] B. Ren, H. Wang, V. O. Kompanets, Y. V. Kartashov, Y. Li, and Y. Zhang, Dark topological valley Hall edge solitons, Nanophotonics **10**, 3559 (2021).
[11] J. K. Asbóth, L. Oroszlány, and A. Pályi, The Su-Schrieffer-Heeger (SSH) model, in *A Short Course on Topological Insulators: Band Structure and Edge States in One and Two Dimensions* (Springer, Cham, 2016), pp. 1–22
[12] Y. Zhang, B. Ren, Y. Li, and F. Ye, Topological states in the super-SSH model, Opt. Express **29**, 42827 (2021).
[13] Y. V. Kartashov, A. A. Arkhipova, S. A. Zhuravitskii, N. N. Skryabin, I. V. Dyakonov, A. A. Kalinkin, S. P. Kulik, V. O. Kompanets, S. V. Chekalin, L. Torner, and V. N. Zadkov, Observation of Edge Solitons in Topological Trimer Arrays, Phys. Rev. Lett. **128**, 093901 (2022).
[14] G. Salerno, T. Ozawa, H. M. Price, and I. Carusotto, How to directly observe Landau levels in driven-dissipative strained honeycomb lattices, 2D Mater. **2**, 034015 (2015).
[15] G. G. Naumis, S. Barraza-Lopez, M. Oliva-Leyva, and H. Terrones, Electronic and optical properties of strained graphene and other strained 2D materials: A review, Rep. Prog. Phys. **80**, 096501 (2017).
[16] M. C. Rechtsman, J. M. Zeuner, A. Tünnermann, S. Nolte, M. Segev, and A. Szameit, Strain-induced pseudomagnetic field and photonic Landau levels in dielectric structures, Nat. Photonics **7**, 153 (2013).
[17] H. Schomerus and N. Y. Halpern, Parity Anomaly and Landau-Level Lasing in Strained Photonic Honeycomb Lattices, Phys. Rev. Lett. **110**, 013903 (2013).
[18] B. Tian, M. Endres, and D. Pekker, Landau Levels in Strained Optical Lattices, Phys. Rev. Lett. **115**, 236803 (2015).
[19] Z. Yang, F. Gao, Y. Yang, and B. Zhang, Strain-Induced Gauge Field and Landau Levels in Acoustic Structures, Phys. Rev. Lett. **118**, 194301 (2017).
[20] O. Jamadi, E. Rozas, G. Salerno, M. Milićević, T. Ozawa, I. Sagnes, A. Lemaître, L. Le Gratiet, A. Harouri, I. Carusotto, J. Bloch, and A. Amo, Direct observation of photonic Landau levels and helical edge states in strained honeycomb lattices, Light: Sci. Appl. **9**, 144 (2020).
[21] M. Bellec, C. Poli, U. Kuhl, F. Mortessagne, and H. Schomerus, Observation of supersymmetric pseudo-Landau levels in strained microwave graphene, Light: Sci. Appl. **9**, 146 (2020).
[22] M. Polini, F. Guinea, M. Lewenstein, H. C. Manoharan, and V. Pellegrini, Artificial honeycomb lattices for electrons, atoms and photons, Nat. Nanotechnol. **8**, 625 (2013).
[23] A. Szameit, M. C. Rechtsman, O. Bahat-Treidel, and M. Segev, $\mathcal{PT}$-symmetry in honeycomb photonic lattices, Phys. Rev. A **84**, 021806(R) (2011).
[24] M. Kremer, T. Biesenthal, L. J. Maczewsky, M. Heinrich, R. Thomale, and A. Szameit, Demonstration of a two-dimensional $\mathcal{PT}$-symmetric crystal, Nat. Commun. **10**, 435 (2019).
[25] M. C. Rechtsman, Y. Plotnik, J. M. Zeuner, D. Song, Z. Chen, A. Szameit, and M. Segev, Topological Creation and Destruction of Edge States in Photonic Graphene, Phys. Rev. Lett. **111**, 103901 (2013).
[26] L. Lu, J. D. Joannopoulos, and M. Soljačić, Topological photonics, Nat. Photonics **8**, 821 (2014).
[27] T. Ozawa, H. M. Price, A. Amo, N. Goldman, M. Hafezi, L. Lu, M. C. Rechtsman, D. Schuster, J. Simon, O. Zilberberg, and I. Carusotto, Topological photonics, Rev. Mod. Phys. **91**, 015006 (2019).
[28] D. Smirnova, D. Leykam, Y. Chong, and Y. Kivshar, Nonlinear topological photonics, Appl. Phys. Rev. **7**, 021306 (2020).
[29] S. Ryu and Y. Hatsugai, Topological Origin of Zero-Energy Edge States in Particle-Hole Symmetric Systems, Phys. Rev. Lett. **89**, 077002 (2002).
[30] P. Delplace, D. Ullmo, and G. Montambaux, Zak phase and the existence of edge states in graphene, Phys. Rev. B **84**, 195452 (2011).

[31] D. Obana, F. Liu, and K. Wakabayashi, Topological edge states in the Su-Schrieffer-Heeger model, Phys. Rev. B **100**, 075437 (2019).

[32] S. Liu, W. Gao, Q. Zhang, S. Ma, L. Zhang, C. Liu, Y. J. Xiang, T. J. Cui, and S. Zhang, Topologically protected edge state in two-dimensional Su-Schrieffer-Heeger circuit, Research **2019**, 8609875 (2019).

[33] G. Montambaux, F. Piéchon, J.-N. Fuchs, and M. O. Goerbig, A universal Hamiltonian for motion and merging of Dirac points in a two-dimensional crystal, Eur. Phys. J. B **72**, 509 (2009).

[34] M. S. Kirsch, Y. Zhang, M. Kremer, L. J. Maczewsky, S. K. Ivanov, Y. V. Kartashov, L. Torner, D. Bauer, A. Szameit, and M. Heinrich, Nonlinear second-order photonic topological insulators, Nat. Phys. **17**, 995 (2021).

[35] D. Tan, Z. Wang, B. Xu, and J. Qiu, Photonic circuits written by femtosecond laser in glass: Improved fabrication and recent progress in photonic devices, Adv. Photonics **3**, 024002 (2021).

[36] L. Li, W. Kong, and F. Chen, Femtosecond laser-inscribed optical waveguides in dielectric crystals: A concise review and recent advances, Adv. Photonics **4**, 024002 (2022).

[37] H. Zhong, S. Xia, Y. Zhang, Y. Li, D. Song, C. Liu, and Z. Chen, Nonlinear topological valley Hall edge states arising from type-II Dirac cones, Adv. Photonics **3**, 056001 (2021).

[38] Q. Fu, P. Wang, C. Huang, Y. V. Kartashov, L. Torner, V. V. Konotop, and F. Ye, Optical soliton formation controlled by angle twisting in photonic moiré lattices, Nat. Photonics **14**, 663 (2020).

[39] Z. Hu, D. Bongiovanni, D. Jukić, E. Jajtić, S. Xia, D. Song, J. Xu, R. Morandotti, H. Buljan, and Z. Chen, Nonlinear control of photonic higher-order topological bound states in the continuum, Light: Sci. Appl. **10**, 164 (2021).

[40] Y. Q. Zhang, Z. K. Wu, M. R. Belić, H. B. Zheng, Z. G. Wang, M. Xiao, and Y. P. Zhang, Photonic Floquet topological insulators in atomic ensembles, Laser Photonics Rev. **9**, 331 (2015).

[41] Z. Y. Zhang, R. Wang, Y. Q. Zhang, Y. V. Kartashov, F. Li, H. Zhong, H. Guan, K. Gao, F. L. Li, Y. P. Zhang, and M. Xiao, Observation of edge solitons in photonic graphene, Nat. Commun. **11**, 1902 (2020).

[42] Z. Chen, X. Liu, and J. Zeng, Electromagnetically induced moiré optical lattices in a coherent atomic gas, Front. Phys. **17**, 42508 (2022).

[43] H.-X. Wang, G.-Y. Guo, and J.-H. Jiang, Band topology in classical waves: Wilson-loop approach to topological numbers and fragile topology, New J. Phys. **21**, 093029 (2019).

[44] S. K. Ivanov, Y. V. Kartashov, A. Szameit, L. Torner, and V. V. Konotop, Vector topological edge solitons in Floquet insulators, ACS Photonics **7**, 735 (2020).

[45] Y. Tian, Y. Zhang, Y. Li, and M. R. Belić, Vector valley Hall edge solitons in the photonic lattice with type-II Dirac cones, Front. Phys. **17**, 53503 (2022).

[46] S. K. Ivanov, Y. V. Kartashov, M. Heinrich, A. Szameit, L. Torner, and V. V. Konotop, Topological dipole Floquet solitons, Phys. Rev. A **103**, 053507 (2021).

[47] Y. V. Kartashov and D. V. Skryabin, Modulational instability and solitary waves in polariton topological insulators, Optica **3**, 1228 (2016).

[48] S. K. Ivanov, Y. V. Kartashov, L. J. Maczewsky, A. Szameit, and V. V. Konotop, Edge solitons in Lieb topological Floquet insulator, Opt. Lett. **45**, 1459 (2020).

[49] Q. Tang, Y. Zhang, Y. V. Kartashov, Y. Li, and V. V. Konotop, Vector valley Hall edge solitons in superhoneycomb lattices, Chaos, Solitons Fractals **161**, 112364 (2022).

[50] Y. Zhang, Y. V. Kartashov, L. Torner, Y. Li, and A. Ferrando, Nonlinear higher-order polariton topological insulator, Opt. Lett. **45**, 4710 (2020).

[51] B. Xie, H.-X. Wang, X. Zhang, P. Zhan, J.-H. Jiang, M. Lu, and Y. Chen, Higher-order band topology, Nat. Rev. Phys. **3**, 520 (2021).

[52] W. Zhang, X. Xie, H. Hao, J. Dang, S. Xiao, S. Shi, H. Ni, Z. Niu, C. Wang, K. Jin, X. Zhang, and X. Xu, Low-threshold topological nanolasers based on the second-order corner state, Light: Sci. Appl. **9**, 109 (2020).

[53] H.-R. Kim, M.-S. Hwang, D. Smirnova, K.-Y. Jeong, Y. Kivshar, and H.-G. Park, Multipolar lasing modes from topological corner states, Nat. Commun. **11**, 5758 (2020).

[54] C. Han, M. Kang, and H. Jeon, Lasing at multidimensional topological states in a two-dimensional photonic crystal structure, ACS Photonics **7**, 2027 (2020).

[55] H. Zhong, Y. V. Kartashov, A. Szameit, Y. Li, C. Liu, and Y. Zhang, Theory of topological corner state laser in kagome waveguide arrays, APL Photonics **6**, 040802 (2021).

[56] Y. Ota, F. Liu, R. Katsumi, K. Watanabe, K. Wakabayashi, Y. Arakawa, and S. Iwamoto, Photonic crystal nanocavity based on a topological corner state, Optica **6**, 786 (2019).

[57] X. Xie, W. Zhang, X. He, S. Wu, J. Dang, K. Peng, F. Song, L. Yang, H. Ni, Z. Niu, C. Wang, K. Jin, X. Zhang, and X. Xu, Cavity quantum electrodynamics with second-order topological corner state, Laser Photonics Rev. **14**, 1900425 (2020).